



ALMA Detections of [O III] and [C II] Emission Lines From A1689-zD1 at $z = 7.13$

Yi Hang Valerie Wong¹, Poya Wang², Tetsuya Hashimoto^{1,3,4}, Toshinobu Takagi⁵, Tomotsugu Goto^{1,6},
Seong Jin Kim¹, Cossas K.-W. Wu⁶, Alvina Y. L. On^{1,3,7}, Daryl Joe D. Santos^{1,8}, Ting-Yi Lu^{1,9}, Ece Kilerci-Eser¹⁰,
Simon C.-C. Ho¹, and Tiger Y.-Y. Hsiao¹

¹ Institute of Astronomy, National Tsing Hua University, 101, Section 2, Kuang-Fu Road, Hsinchu, 30013, Taiwan (R.O.C.); valeriew510@gmail.com

² Department of Physics, Tamkang University, New Taipei City 251301, Taiwan (R.O.C.)

³ Centre for Informatics and Computation in Astronomy (CICA), National Tsing Hua University, 101, Section 2, Kuang-Fu Road, Hsinchu, 30013, Taiwan (R.O.C.)

⁴ Department of Physics, National Chung Hsing University, No. 145, Xingda Road, South District, Taichung, 40227, Taiwan (R.O.C.)

⁵ Japan Space Forum, Shin-Ochanomizu Urban Trinity Building 3F, 3-2-1, Kandasurugadai, Chiyoda-ku, Tokyo 101-0062, Japan

⁶ Department of Physics, National Tsing Hua University, 101, Section 2, Kuang-Fu Road, Hsinchu, 30013, Taiwan (R.O.C.)

⁷ Mullard Space Science Laboratory, University College London, Holmbury St. Mary, Dorking, Surrey RH5 6NT, UK

⁸ Max Planck Institute for Extraterrestrial Physics, Gießenbachstraße 1, D-85748 Garching, Germany

⁹ Cosmic Dawn Center, Niels Bohr Institute, University of Copenhagen, Jagtvej 128 DK-2200 Copenhagen N, Denmark

¹⁰ Sabancı University, Faculty of Engineering and Natural Sciences, 34956, Istanbul, Turkey

Received 2021 September 29; revised 2022 February 12; accepted 2022 February 16; published 2022 April 26

Abstract

A1689-zD1 is one of the most distant galaxies, discovered with the aid of gravitational lensing, providing us with an important opportunity to study galaxy formation in the very early universe. In this study, we report the detection of [C II]158 μm and [O III]88 μm emission lines of A1689-zD1 in the Atacama Large Millimeter/submillimeter Array (ALMA) Bands 6 and 8. We measure the redshift of this galaxy as $z_{\text{sys}} = 7.133 \pm 0.005$ based on the [C II] and [O III] emission lines, consistent with that adopted by Bakx et al. The observed $L_{[\text{O III}]} / L_{[\text{C II}]}$ ratio is 2.09 ± 0.09 , higher than that of most of the local galaxies, but consistent with other $z \sim 7$ galaxies. The moderate spatial resolution of ALMA data provided us with a precious opportunity to investigate spatial variation of $L_{[\text{O III}]} / L_{[\text{C II}]}$. In contrast to the average value of 2.09, we find a much higher $L_{[\text{O III}]} / L_{[\text{C II}]}$ of ~ 7 at the center of the galaxy. This spatial variation of $L_{[\text{O III}]} / L_{[\text{C II}]}$ was seldom reported for other high- z galaxies. It is also interesting that the peak of the ratio does not overlap with optical peaks. Possible physical reasons include a central active galactic nucleus, shock heating from merging, and a starburst. Our moderate spatial resolution data also reveal that in addition to the observed two clumps shown in previous Hubble Space Telescope images, there is a redshifted segment to the west of the northern optical clump. This structure is consistent with previous claims that A1689-zD1 is a merging galaxy, but with the northern redshifted part being some ejected material, or that the northern redshifted material stems from a third more highly obscured region of the galaxy.

Unified Astronomy Thesaurus concepts: [High-redshift galaxies \(734\)](#); [Galaxy kinematics \(602\)](#); [Emission line galaxies \(459\)](#); [Submillimeter astronomy \(1647\)](#)

1. Introduction

Studies of high-redshift (high- z) galaxies are crucial for understanding the early phase of galaxy formation and evolution. The gravitationally lensed galaxy A1689-zD1 is one of the most distant sources ($z \sim 7.13$) discovered so far; it is strongly lensed by a factor of $\mu = 9.3$ (Bradley et al. 2008). It is therefore a useful probe to study the early universe. Recently, Bakx et al. (2021) adopted a new redshift of the galaxy $z = 7.13$, and our measurement confirms the redshift.

Having a high dust mass as compared to the Milky Way makes A1689-zD1 unusual among high-redshift dust emitters. It is also a sub- L^* galaxy (Watson et al. 2015). The massive amount of dust may indicate a gas-rich system that makes the emission lines from the interstellar medium (ISM) detectable. According to Bradley et al. (2008), A1689-zD1 is a system composed of two clumps, which are likely separate star-forming regions within the galaxy, but they could conceivably be interpreted as small star-forming galaxies merging at high redshift.

Previously, A1689-zD1 was detected in the dust continuum with the Atacama Large Millimeter/submillimeter Array (ALMA) in the absence of emission lines (Knudsen et al. 2017; Bakx et al. 2021), except for a slight excess in [C II]158 μm (Knudsen et al. 2017). Using the dust continuum, the sizes of the two detected clumps were estimated to be 0.4–1.7 kpc, and the dust temperature was approximated to be $T_{\text{dust}} \sim 35\text{--}45$ K. A recent update of the dust temperature and mass of A1689-zD1 using the continuum estimated with the [C II]-based method is $T_{\text{dust}} = 40_{-7}^{+13}$ K and $M_{\text{d}} = 2.0_{-1.0}^{+1.8} \times 10^7 M_{\odot}$ (Bakx et al. 2021).

In Watson et al. (2015), the redshift was measured from the X-shooter spectra taken on the Very Large Telescope, using the Lyman break due to the lack of $\text{Ly}\alpha$ and other emission lines. However, the redshift measurement based on the Lyman break is less certain than that using high-excitation lines. Moreover, the break is close to the spectrograph's near-infrared/visual arm split. Thus, the redshift needs to be measured more accurately. Using [C II] and [O III] emission lines, the redshift of 7.13 by spectral measurement adopted by Bakx et al. (2021) is confirmed in this work.

Since [O III]88 μm is bright for some galaxies at $z > 6$ (e.g., Inoue et al. 2016; Carniani et al. 2017; Harikane et al. 2020), the [O III] line is one of the most useful tracers of ISM

Table 1
Observational Configurations

	Band 6 [C II]158 μm	Band 8 [O III]88 μm
Baseline lengths (m)	15–1605	15–784
Number of antennas	38–40	41–47
Spectral window 1 (GHz)	217.17–219.05	404.48–406.30
Spectral window 2 (GHz)	219.05–220.93	406.31–408.14
Spectral window 3 (GHz)	231.96–233.84	416.33–418.20
Spectral window 4 (GHz)	233.85–235.73	418.18–420.01
Channel width (MHz)	1.95	3.91
Exp. time on source (hour)	7.81	3.43
PWV (mm)	0.3–1.1	0.3–1.0
MRS (arcsec)	5.32	4.58

Note. The PWV values for each of the band data are from separate measurement sets due to the long exposure time; therefore, we present the minimum and maximum of averages per execution block (EB).

properties. In addition, [O III] has a higher ionization potential (35.1 eV) than [C II] (11.3 eV). Therefore, the [O III]/[C II] ratio is useful to investigate the ionization state.

In this paper, we present an analysis of archival ALMA data of [C II]158 μm and [O III]88 μm in Cycles 3 and 5 with a higher spatial resolution ($\sim 0''.2$) than ever before ($\sim 0''.9$ Knudsen et al. 2017; $0''.6$ – $0''.7$ Watson et al. 2015). With this higher spatial resolution, the data can be used to examine the line emissions, to resolve structures inside the galaxy, and to investigate velocity structures and so on in comparison with the Hubble Space Telescope (HST) images. For example, this higher spatial resolution allows us to examine the kinematic properties of A1689-zD1. We can also investigate the ratio of [O III]/[C II] as a function of positions within the galaxy. This is important because, as some previous studies discussed, the observed high [O III]/[C II] may be due to the difference in their spatial distributions (Carniani et al. 2017).

This paper is organized as follows. In Section 2 we describe the ALMA data set used in the study; Section 3 presents the main results, and discussions are provided in Section 4. Finally, we present our conclusions in Section 5. Throughout this paper, we assume the Planck15 cosmology (Planck Collaboration et al. 2016) as a fiducial model, i.e., a Λ cold dark matter cosmology with $(\Omega_m, \Omega_\Lambda, \Omega_b, h) = (0.308, 0.682, 0.0486, 0.678)$.

2. Observation

Two ALMA bands, Bands 6 and 8, are chosen in this study in order to characterize the physical properties of A1689-zD1. Because it is a dusty galaxy (Watson et al. 2015), it is important to measure the star formation rate (SFR) derived from far-infrared (FIR) observations, using its relation with [C II]158 μm and [O III]88 μm emissions. At the redshift of A1689-zD1, Band 6 covers the [C II] emission line, and Band 8 covers the [O III] emission line.

The Band 6 observation was carried out in 2016 from August 1 to 25 (Cycle 3) with the ALMA 12 m array and an antenna configuration of C36-(4)/5 and C36-(5)/6 (project ID: 2015.1.01406.S, P.I.: D. Watson), while the Band 8 data were obtained from observations in 2018 from April to December (Cycle 5), also with the 12 m array, but in an antenna configuration of C43-3 and C43-4 (project ID: 2017.1.00775.S,

P.I.: D. Watson). The observational configurations are summarized in Table 1.

The calibration of visibility data from the ALMA archive was conducted with the pipeline versions 4.7 and 5.4 for Bands 6 and 8, respectively, provided by the ALMA project using the Common Astronomy Software Applications (CASA). For the Band 6 data, targeting [C II], the channel width of the observation is 1.95 MHz. For the Band 8 data, targeting [O III], the channel width is 3.91 MHz. The total exposure time on source for the Band 6 ([C II]) observation is 28,123 s \sim 7.81 hr, while that for the Band 8 ([O III]) observation is 12,337 s \sim 3.43 hr. The maximum recoverable scales (MRS) for the Band 6 and Band 8 data are $5''.32$ and $4''.58$, respectively, which are larger than the detected signals, as we discuss below.

Using the calibrated measurement set (MS), we create image cubes for the [C II] and [O III] lines with a spectral resolution of 10 km s^{-1} . The beam size is controlled by the robustness parameter of the Briggs weighting and uv -tapering in the CASA task `tclean()`. First, we subtract the continuum in each band using the CASA task `uvcontsub` by selecting the frequency ranges without line detection, i.e., 232.000 \sim 233.420 GHz for Band 6, and 416.342 \sim 416.823 GHz and 417.588 \sim 418.178 GHz for Band 8. Next, in order to investigate both the morphology and photometry of A1689-zD1, we produce two sets of image cubes for each of the bands (Hashimoto et al. 2019a). Since we are interested in the extent of [C II] and [O III] emissions of the galaxy, we adopt a Briggs robust weighting of $R = 0.5$, achieving a beam size of $0''.271 \times 0''.243$ ($0''.387 \times 0''.332$), with a position angle at -80° (-89°) for Band 6 (8) data. As presented in Section 3.1.1, the extended structure does not exceed the MRS in the two bands. Hence, we use the image cube sets with Briggs robust parameter $R = 0.5$ for the morphology analysis of A1689-zD1. To maximize the sensitivity of collecting the flux as a point source, we use natural weighting by setting $R = 2$, and further apply uv -tapering to $2''$ so as to obtain the maximum flux of the extended source. The beam size is dramatically increased to $2''.640 \times 2''.337$ ($1''.874 \times 1''.790$) at -63° (-70°) for Band 6 (8) data. This set of data is used for flux and related calculations of the galaxy. The characteristics of the calibrated images are summarized in Table 2.

3. Results

3.1. [C II] and [O III] Emission Lines

3.1.1. Spatial Distribution

Using the CASA task `immoments`, we obtain moment-0 maps of the Band 6 and Band 8 (Briggs) data by stacking the cube channels along the spectrum, covering $\sim 400 \text{ km s}^{-1}$ (~ 1.2 FWHM). This is done to ensure that the detections of the emission lines are valid (Novak et al. 2019). This range of frequency is comparable to that in previous studies (Inoue et al.

2016; Matthee et al. 2017; Hashimoto et al. 2019b; Novak et al. 2019). Figure 1 shows the [C II] (white contours) line emission at 3, 7, 11, and 15 σ levels and the [O III] (magenta contours) line emission at 3, 7, 11, 15, and 19 σ levels, overlaid on the combined HST color image. For the purpose of color display, we stack the HST filters with F105W as blue, F125W as green, and F160W as red (proposal ID: 11802, P.I.: Ford). There is a known coordinate offset between their ALMA image and HST image as an average value of $0''.4 \sim 0''.45$ (Watson et al. 2015). We therefore measure the position difference of the peaks between the ALMA Bands 6 and 8 data and the HST image we use, and shift the ALMA contours by $0''.386$ along

Table 2
Summary of Image Characteristics

	Band 6 (Briggs)	Band 6 (Natural and uv -tapered)	Band 8 (Briggs)	Band 8 (Natural and uv -tapered)
Beam major/minor axes (arcsec)	0.271/0.243	2.640/2.337	0.387/0.332	1.874/1.790
Beam position angle ^a (deg)	-80	-63	89	-70
Sensitivity ^b (mJy beam ⁻¹)	0.17	0.59	0.66	1.69

Notes.

^a The beam PA is in degrees east of north, by which the major axis is rotated.

^b Sensitivity is defined as the rms value of the cube image with 10 km s⁻¹ channel width.

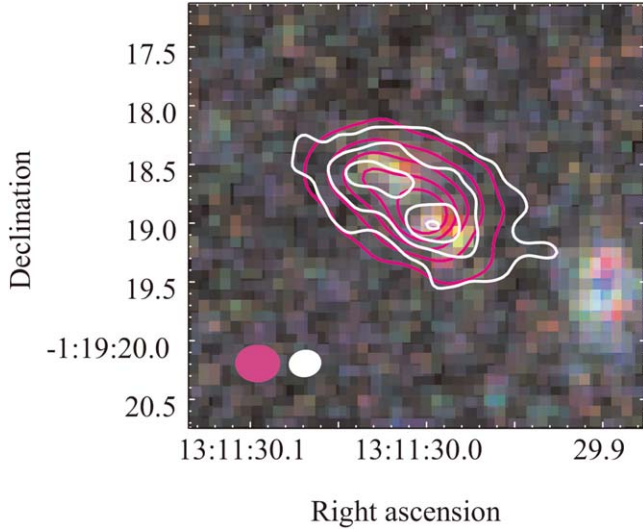


Figure 1. [C II] (white) contours are drawn at 3, 7, 11, and 15 σ levels ($\sigma_{[\text{C II}]} \sim 17.1$ mJy beam⁻¹ km s⁻¹), while [O III] (magenta) contours are drawn at 3, 7, 11, 15, and 19 σ levels ($\sigma_{[\text{O III}]} \sim 55.7$ mJy beam⁻¹ km s⁻¹). Overlaid is a $\sim 3''.5 \times 3''.5$ cutout image of HST data composed of images using the filters F105W (blue), F125W (green), and F160W (red). The corresponding beam sizes of the Briggs Band 6 and Band 8 images used are $0''.271 \times 0''.243$ at -80° and $0''.387 \times 0''.332$ at 89° , respectively.

right ascension (R.A.) in order to match the peaks for a better comparison. Because the structures shown in Figure 1 extend to a 3σ detection that is within an area of $\sim 2''.3 \times 1''.5$ for both [C II] and [O III], which is much smaller than the MRS of $5''.32$ and $4''.58$ for [C II] and [O III], respectively, we confirm that the observed structures are not artificial. Both [C II] and [O III] emission lines are spatially well resolved with angular resolutions of $0''.203$ and $0''.232$, respectively.

From the HST image shown in Figure 1, we see that there are two clumps: one in the northeast (clump A), and one in the southwest (clump B). We refer to them as clump A and clump B throughout.

3.1.2. Spectra

Using elliptical apertures of $8''.5 \times 7''.5$ and $6''.5 \times 5''.5$ (both approximately 3 beams), we extracted spectra from the natural and uv -tapered Band 6 and Band 8 image cubes, respectively. The spectra are shown in blue in Figure 2. This is to include all the flux obtainable by covering the area within which spatially extended emission may exist, for instance, the [C II] $158 \mu\text{m}$ halos around $z \sim 6$ galaxies reported by Fujimoto et al. (2019). At around the rest frequencies of [C II] $158 \mu\text{m}$ and [O III] $88 \mu\text{m}$, in Band 6 and Band 8 respectively, we detect a line

emission with two peaks in each band, indicated as “redshifted” and “blueshifted”, as shown in Figure 2. They may indicate two merging components. More analyses are presented in Sections 3.2 and 3.3. Here, we first fit the spectra with two Gaussians. We obtain two peaks of Gaussians centered at 233.58 ± 0.05 GHz and 233.72 ± 0.08 GHz for [C II] using Band 6 data in panel (a). Similarly, for Band 8 data, we find two peaks of [O III] at 416.98 ± 0.08 GHz and 417.23 ± 0.11 GHz, respectively, after applying a two-Gaussian fitting, as shown in panel (b). The fitted results are shown as dotted red lines in Figure 2. We acquire a redshift of $z_{[\text{C II}]_{\text{red}}} = 7.137 \pm 0.002$ for the redshifted part and a redshift of $z_{[\text{C II}]_{\text{blue}}} = 7.132 \pm 0.003$ for the blueshifted part for the [C II] line detections in Band 6. Accordingly, we obtain redshifts of $z_{[\text{O III}]_{\text{red}}} = 7.137 \pm 0.002$ and $z_{[\text{O III}]_{\text{blue}}} = 7.132 \pm 0.002$ with Band 8 [O III] detections for the redshifted and blueshifted parts. We find that the redshifts we obtain from the [C II] and [O III] line detections agree well with each other for the two components.

The signal-to-noise ratio (S/N), defined as the ratio of the peak flux of the source (moment-0 map) to the background noise of the image, is calculated for both Band 6 and Band 8 (natural and uv -tapered) data, with a value of S/N = 51.5 for [C II] and S/N = 22.3 for [O III]. Note that for Briggs-weighted data, the S/N values are calculated as 16.1 for [C II] and 27.9 for [O III].

Taking the average of the redshifts obtained from [Cii] and [Oiii] spectra, we obtain a systemic redshift $z_{\text{sys}} = 7.133 \pm 0.005$. This matches the adopted redshift $z = 7.13$ in Bakx et al. (2021). The new redshift derived from FIR fine structure [C II] and [O III] lines, and hence is a better measurement than the previous estimate of $z \sim 7.5$ based on the Lyman break with no detection of any emission line (Watson et al. 2015).

We measure the widths of the emission lines with their FWHMs in terms of velocity (km s⁻¹). Details of the measured and derived parameters, corrected with a lensing magnification factor of $\mu = 9.3$ (Bradley et al. 2008), of the galaxy, are summarized in Table 3. We also include the 1σ uncertainty of the parameters in Table 3. The emission-line fluxes of [C II] and [O III] are measured by integrating the flux density along the velocity, obtaining a total of 548 ± 56 mJy km s⁻¹ for [C II], and 640 ± 69 mJy km s⁻¹ for [O III]. We note that each flux error mentioned above is calculated by a quadrature sum of (i) the fitting error of the emission line and (ii) the 10% error due to the uncertainty in the absolute flux scale of ALMA data. With total line fluxes and systemic redshift deduced, we derive the line luminosities with the equation

$$L_{\text{line}} = 1.04 \times 10^{-3} \times \left(\frac{S_{\text{line}} \Delta v}{\text{Jy km s}^{-1}} \right) \left(\frac{D_L}{\text{Mpc}} \right)^2 \left(\frac{\nu_{\text{obs}}}{\text{GHz}} \right) L_{\odot} \quad (1)$$

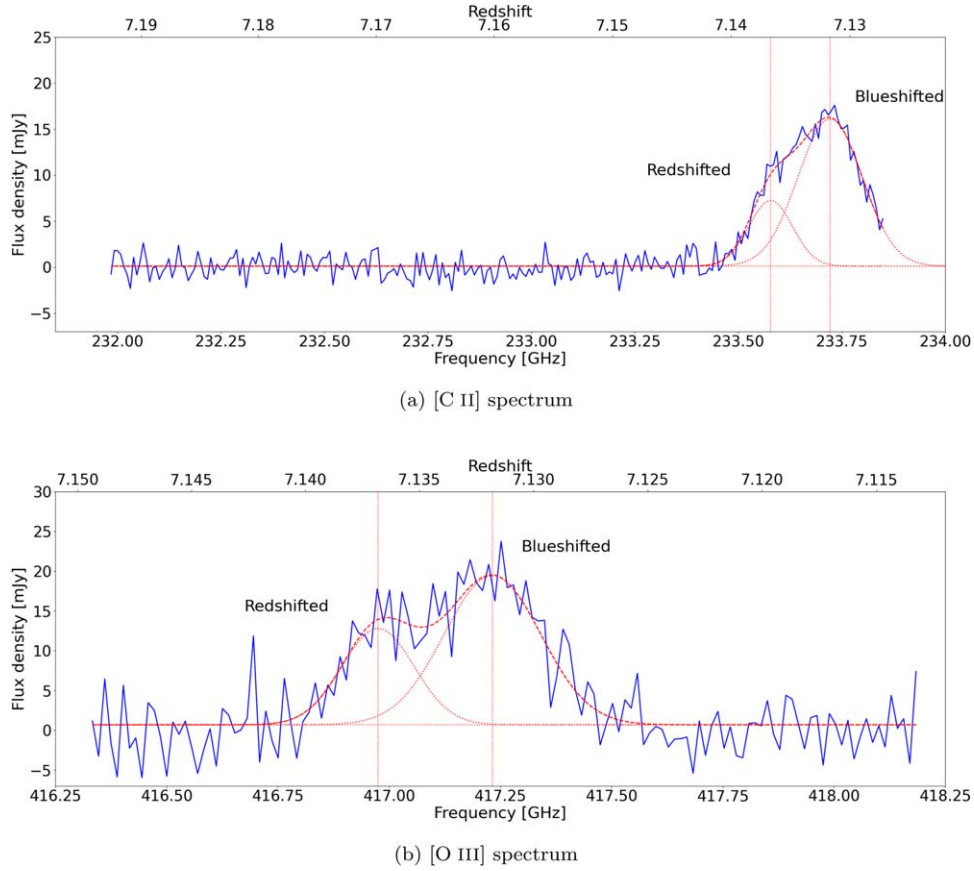


Figure 2. Spectra of (a) [C II]158 μm and (b) [O III]88 μm using ALMA (a) Band 6 and (b) Band 8 data (natural and uv -tapered). The dotted red lines in each panel show the Gaussian fitting results of clumps A and B, as indicated.

Table 3
Measured and Derived Parameters of A1689-zD1, Corrected for Lensing Magnification ($\mu = 9.3$)

Peak	[C II]158 μm		[O III]88 μm	
	Redshifted	Blueshifted	Redshifted	Blueshifted
Central frequency (GHz)	233.58 ± 0.05	233.72 ± 0.08	416.98 ± 0.08	417.23 ± 0.11
Redshift	7.137 ± 0.002	7.132 ± 0.003	7.137 ± 0.002	7.132 ± 0.002
Emission-line width (km s^{-1})	150 ± 20	237 ± 19	122 ± 21	211 ± 21
Total emission-line width (km s^{-1})		323 ± 8		311 ± 17
Emission-line flux (mJy km s^{-1})	124 ± 13	423 ± 43	165 ± 18	475 ± 53
Total line flux (mJy km s^{-1})		548 ± 56		640 ± 69
Luminosity ($10^7 L_{\odot}$)	15.7 ± 1.6	53.5 ± 5.5	37.2 ± 4.2	107.3 ± 12.0
Total luminosity ($10^7 L_{\odot}$)		69.2 ± 7.0		144.5 ± 15.5

Note. *All errors are shown in 1σ . ** “Emission-line width,” “emission-line flux,” and “luminosity” indicate those of separate components derived by the spectral fitting analysis, while “total emission-line width,” “total line flux,” and “total luminosity” indicate those of the redshifted and blueshifted line emission as a whole. *** For the errors of fluxes and luminosities, both the fitting errors and the 10% errors due to the absolute calibration uncertainty of ALMA data are taken into consideration.

(Weinberg 1972; Solomon et al. 1992; Carilli & Walter 2013), where $S_{\text{line}}\Delta\nu$ is the measured flux of the line, D_L is the luminosity distance, and ν_{obs} is the observed frequency. The total luminosity of [C II] we obtained is $(69.2 \pm 1.2) \times 10^7 L_{\odot}$, and that of [O III] is $(144.5 \pm 5.7) \times 10^7 L_{\odot}$. The obtained $L_{[\text{C II}]}$ is slightly different from the value of $(6.1 \pm 0.7) \times 10^8 L_{\odot}$ adopted by Bakx et al. (2021) by nearly 1σ . Possible reasons may include different integration regions, beam sizes of the images, the parameter settings of the uv -tapering, and/or different frequency ranges included.

3.2. [O III]/[C II] Ratio and Luminosity

$L_{[\text{C II}]}$ and $L_{[\text{O III}]}$ are calculated using the derived redshift of $z = 7.133 \pm 0.005$, so that $L_{[\text{C II}]} = (69.2 \pm 1.2) \times 10^7 L_{\odot}$ and $L_{[\text{O III}]} = (144.5 \pm 5.7) \times 10^7 L_{\odot}$. We therefore obtain a total [O III]-to-[C II] luminosity ratio of 2.09 ± 0.09 .

With the obtained $L_{[\text{C II}]}$, we can also revise the SFR of the system using the relation

$$\text{SFR}_{[\text{C II}]} = 1.0 \times 10^{-7} \left(\frac{L_{[\text{C II}]}}{L_{\odot}} \right)^{0.98}, \quad (2)$$

based on De Looze et al. (2011), who assumed a Kroupa initial mass function (IMF; Kroupa 2001). We obtain an $\text{SFR}_{[\text{C II}],\text{Krou}} = 46.1 \pm 0.8 M_{\odot} \text{ yr}^{-1}$. In Bakx et al. (2021), however, their dust-obscured SFR was derived from an IR luminosity-to-SFR relation that assumed a Salpeter IMF, with an estimated value of $\text{SFR}_{\text{obsc,Sal}} = 33 \pm 9 M_{\odot} \text{ yr}^{-1}$. In order to compare the SFR value we obtain with that derived in Bakx et al. (2021), we divide our SFR value by a factor of 0.67 to convert it into a Salpeter IMF-based SFR (Madau & Dickinson 2014); thus, it becomes $\text{SFR}_{[\text{C II}],\text{Sal}} = 68.8 \pm 1.2 M_{\odot} \text{ yr}^{-1}$. This value is about twice the value derived by Bakx et al. (2021). The exact reason for the difference is not clear. Possible reasons include (1) that the relation from De Looze et al. (2011) was derived from photometric data corrected for attenuation, while Bakx et al. (2021) derived the SFR from an SED-fitting result, (2) the temperature dependence of the [C II]–SFR relation (Malhotra et al. 1997), and/or (3) the uncertainty in the SED fitting due to the limited FIR photometric coverage. Additional further FIR data points would improve the SED fitting. Despite the difference, according to the bottom panel of Figure 3 in De Looze et al. (2011), the logarithmic difference between the SFR derived from attenuation and that from the [C II] line is still within a reasonable range. De Looze et al. (2011) presented almost an order of magnitude scatter on the SFR–[C II] relation, along with detailed discussions.

We show the [O III]/[C II] luminosity ratio map overlaid by black contours of the [C II] emission-line flux at 3, 7, 11, and 15 σ levels, and magenta contours of the [O III] emission-line flux at 3, 7, 11, 15, and 19 σ levels in Figure 3.

In order to make a comparison between the two emissions, we need to enlarge the beam size of the Band 6 [C II] data to that of the Band 8 [O III] data before taking the ratio. Therefore, we apply a uv -tapering in the CASA task `tclean()` to the [C II] Briggs image to reach a spatial resolution that roughly matches that of the [O III] Briggs image, and further match the synthesized beam size and position angle of the [O III] cube exactly with the `tclean()` parameter `restoringbeam`. After matching the beam size of [C II] data to that of [O III] data, we use the python package `reproject` to reproject the finer pixel size of [C II] data from from $(0''.035 \text{ pix}^{-1} \times 0''.035 \text{ pix}^{-1})$ to $(0''.060 \text{ pix}^{-1} \times 0''.060 \text{ pix}^{-1})$, in order to match that of [O III] data $(0''.060 \text{ pix}^{-1} \times 0''.060 \text{ pix}^{-1})$. Then, we divided the two arrays and re-created the [O III]/[C II] ratio map.

This is one of the rare cases that a spatial distribution of the [O III]/[C II] map is revealed at $z > 7$. Interestingly, the [O III]/[C II] ratio is highest around the center of the galaxy with a value of ~ 7 , and it gradually decreases toward the outer parts of the galaxy, reaching a ratio of one. We further discuss the implications in Section 4.1.

In Figure 4 we show the [O III]/[C II] luminosity ratio as a function of the bolometric luminosity, which is defined as the summation of the UV and total infrared (TIR) luminosities, i.e., $L_{\text{bol}} = L_{\text{UV}} + L_{\text{TIR}}$ (Hashimoto et al. 2019a; Harikane et al. 2020). For comparisons, we also plot the ratios for $z = 6-9$ galaxies in the literature plotted in Carniani et al. (2020) before applying surface brightness dimming (SBD), as well as those of local galaxies studied in the Dwarf Galaxy Survey (Madden et al. 2013; De Looze et al. 2014; Cormier et al. 2015) and the

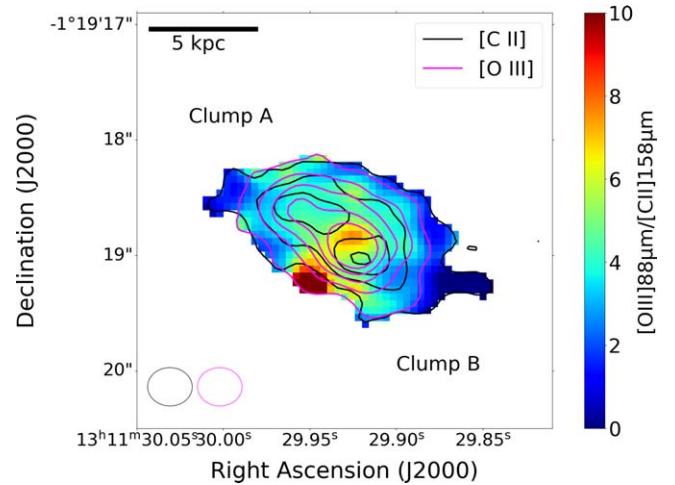


Figure 3. The [O III]88 μm to [C II]158 μm ratio map. Black contours show [C II]88 μm line emission, while magenta contours show [O III] emission. [C II] contours are shown at 3, 7, 11, and 15 σ levels, where $\sigma_{[\text{C II}]} \sim 17.1 \text{ mJy beam}^{-1} \text{ km s}^{-1}$. [O III] contours are shown at 3, 7, 11, 15, and 19 σ levels, where $\sigma_{[\text{O III}]} \sim 55.7 \text{ mJy beam}^{-1} \text{ km s}^{-1}$. The color bar shows the value of [O III] to [C II] luminosity ratio. The smaller beam size $(0''.271 \times 0''.243)$ and finer pixel size $(0''.035 \text{ pix}^{-1} \times 0''.035 \text{ pix}^{-1})$ of the corresponding Band 6 (Briggs) are enlarged to $(0''.387 \times 0''.332; 0''.060 \text{ pix}^{-1} \times 0''.060 \text{ pix}^{-1})$ to match those of the Band 8 data (Briggs). The pixels with [C II] and [O III] fluxes lower than 3 σ are masked out. The resulting beam sizes are shown in the lower left corner of the figure.

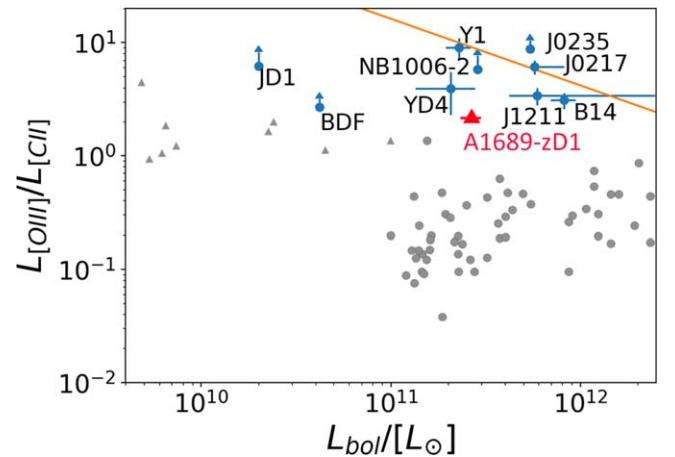


Figure 4. [O III]88 μm /[C II]158 μm luminosity ratio as a function of bolometric luminosity. The red triangle shows the data point for A1689-zD1. The bolometric luminosities of $z = 6-9$ galaxies are taken from Hashimoto et al. (2019a), while the orange line is adopted from Equation (7) in Harikane et al. (2020), which is the fitting function of $z = 6-9$ galaxies. The gray triangle and circles denote $z \sim 0$ galaxies from the Dwarf Galaxy Survey (Madden et al. 2013; De Looze et al. 2014; Cormier et al. 2015) and from the Great Observatories All-sky LIRG Survey (GOALS: Howell et al. 2010; Díaz-Santos et al. 2017), respectively. The bolometric luminosity is estimated as the total of the UV and TIR luminosities.

Great Observatories All-sky LIRG Survey (GOALS: Howell et al. 2010; Díaz-Santos et al. 2017). The orange line is the fitting function of $z = 6-9$ galaxies without A1689-zD1, adopted from Equation (7) in Harikane et al. (2020), as a comparison. Although as suggested in Carniani et al. (2020), SBD may affect the flux measurements gravely with ALMA, we do not apply the same correction because of the high S/N of [C II] emission of A1689-zD1 (~ 17.1). Such an effect was predicted to be weak at high S/N (Carniani et al. 2020). We

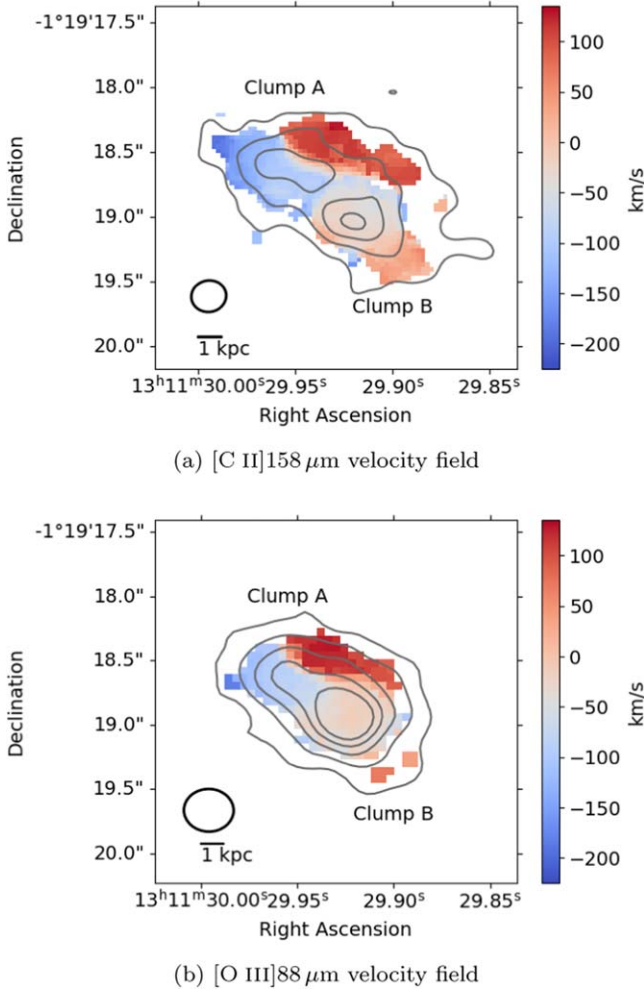


Figure 5. The velocity field (moment-1 map) of the emission lines (top: [C II] 158 μm , and bottom: [O III] 88 μm ; using Briggs-weighted data). The gray contour in the top (bottom) panel is the same as the white (magenta) contour for [C II] ([O III]) emission in Figure 1. The color bar in each panel shows the velocity in the range of $-225 \text{ km s}^{-1} \sim 135 \text{ km s}^{-1}$, as it is close to and covers the maximum and minimum values of both emissions.

find that A1689-zD1 and other $z = 6-9$ galaxies show systematically higher [O III]/[C II] ratios than most of the local galaxies, which is consistent with previous results (Inoue et al. 2016; Laporte et al. 2019).

3.3. Velocity Fields

In this section, we investigate the kinematic properties of A1689-zD1 using [O III] and [C II] emissions. With the CASA task `immoments`, we create flux-weighted velocity (i.e., moment-1) maps of [C II] and [O III] emission lines (Figure 5), using pixels with $>2\sigma$ detections of Briggs data. Note that we do not consider the beam-smearing effect for the velocity fields.

Comparing clumps A and B we observe in Figure 1, we see that clump A consists of a blueshifted component on the upper left (east side) and a redshifted component on the upper right (west side), while clump B is a cloud of a redshifted and blueshifted mixture, but not as intense as the components in clump A.

We only investigate the [C II] field because (1) the Band 6 data ([C II]) have a better S/N than Band 8 data ([O III]), and

(2) the patterns and the values of velocity field in [C II] and [O III] are similar.

A1689-zD1 might be a merger due to the parallel isovelocity lines found between clump A and clump B, as has been claimed (Bradley et al. 2008; Knudsen et al. 2017). A comparison to Figure 1 shows that the two peaks of [C II] are consistent with clump B and the blueshifted part of clump A, while the redshifted part of clump A might be (1) some ejected material from the merger, or (2) material from a highly obscured component of the galaxy. Similar discussions can be found in Jones et al. (2017) and Hashimoto et al. (2019a), while further comparisons to other targets are presented in Section 4.2.

4. Discussion

4.1. High [O III]/[C II] Luminosity Ratio

From Section 3.2, we find a high [O III]/[C II] luminosity ratio of 2.17 ± 0.14 . In the literature (e.g., Carniani et al. 2017; Laporte et al. 2019; Bakx et al. 2020), the [O III]/[C II] luminosity ratios of the $6 < z < 9$ galaxies have been found to be systematically higher than those of $z \sim 0$ galaxies, similar to A1689-zD1. Formerly, Harikane et al. (2020) also found high values of the ratio for their large samples of high- z galaxies.

From their simulations in Katz et al. (2022), when they assume a low C/O abundance, their core-collapse supernova model agrees well with observations with high [O III]/[C II] luminosity ratios at high redshift. Therefore, a low C/O abundance may account for the high [O III]/[C II] ratios for $z \sim 6$ galaxies.

Moreover, as mentioned in Carniani et al. (2020), there might also be an underestimation of [C II] flux caused by high angular resolution. Often, [C II] emission is more spatially extended, and thus, such extended flux might be underestimated due to the interferometric nature of ALMA, which is why we further perform *uv*-tapering so as to increase the beam size of Band 6 data to $\sim 2''$, with a peak S/N of 17.1. Comparing our results with those in Carniani et al. (2020), the value of $L_{[\text{O III}]} / L_{[\text{C II}]} = 2.09 \pm 0.09$ of A1689-zD1 just touched the lower limit of the range of $2 < L_{[\text{O III}]} / L_{[\text{C II}]} < 8$ measured with the nine observed high- z galaxies reported in Carniani et al. (2020). The comparatively high values of $L_{[\text{O III}]} / L_{[\text{C II}]}$ for the other $z > 6$ sources may possibly be due to observational limitations. Carniani et al. (2020) found that for the nine $z > 6$ galaxies, up to 40% of the extended [C II] component might be missed at an ALMA angular resolution of $0''.8$, implying that $L_{[\text{C II}]}$ might be underestimated by a factor of ~ 2 in data at low S/N (< 7).

In the models presented in Harikane et al. (2020), they suggested several possible mechanisms responsible for the high ratio of [O III]/[C II] luminosities that might match the case for the galaxy: (1) a higher ionization parameter (U_{ion}) in higher-redshift galaxies, possibly due to the low-metallicity young stellar populations with larger volumes of [H II] regions; (2) a low photodissociation region (PDR) covering fraction C_{PDF} , with the definition being

$$C_{\text{PDF}} = \frac{\text{No. of sightlines with PDRs}}{\text{No. of sightlines with H II regions}}, \quad (3)$$

where $C_{\text{PDF}} = 0$ gives a decrease of $L_{[\text{C II}]}$ by $\sim 99\%$; and (3) a low C/O ratio due to a young stellar age. Since a higher U_{ion} gives rise to a more extended H II and thus [O III] region

(Figure 15(b) of Harikane et al. 2020), it may not be able to explain the observed sharp peak of [O III] at the center of A1689-zD1. A low C_{PDF} leads to a low [C II] luminosity. While it is impossible that no PDR overlaps the H II region ($C_{\text{PDF}} = 0$), a low coverage of the PDR region ([C II] emission) together with a concentrated H II region may still explain the peaky [O III] as observed in Figure 3. A low C/O ratio due to production of C at a young stellar age may partially explain the high [O III]/[C II] ratio. But it does not indicate the spatial distribution of the ratio.

From Figure 4, most of the discovered high- z galaxies ($z = 6-9$) have an overall $L_{[\text{O III}]} / L_{[\text{C II}]}$ higher than that of A1689-zD1 (~ 2). Thus, we expect that other $z \sim 7$ galaxies might obtain even higher values of the luminosity ratio [O III]/[C II] at the center if they are observed with higher spatial resolution.

In addition, in Figure 3, we find that the [O III]/[C II] ratio is highest in between the optical peaks shown in the HST images (clumps A and B; Figure 1), but not at the peaks, with a ratio of ~ 7 , it then gradually decreases outward. This is a high value as compared to an average luminosity ratio of $L_{[\text{O III}]} / L_{[\text{C II}]} = 2.09 \pm 0.09$. Thanks to the high spatial resolution of our ALMA data, we have the precious opportunity to investigate the spatial variation of the ratio within the galaxy.

A number of physical mechanisms could cause the high ratio at the center of the galaxy. If a central active galactic nucleus (AGN) is present, the ionization of neutral gas by an AGN may be one reason (Walter et al. 2018). Alternatively, if clumps A and B are in the process of merging, the excess [O III] may also be the heated ionized gas due to shock heating from mergers (Hopkins et al. 2007; Minsley et al. 2020). However, we might expect an extended shock front in this case, rather than the point-like high-ratio region we observe in Figure 3. The velocity difference between clumps A and B is also small, at least in the line-of-sight direction. Another explanation may be that A1689-zD1 has a central starburst region that gives rise to ionized gas (Silk 1997). However, this may not be the case for the sharp peak of [O III]/[C II] in A1689-zD1 because according to Weilbacher et al. (2018), ionized gas is diffuse in the H II region of starburst galaxies.

4.2. Velocity Fields

The complexity of the velocity field of the galaxy A1689-zD1 shown in Figure 5 gives little indication of any existence of a rotating disk. We therefore, suggest that it may simply be a merging system, in agreement with previous analyses (e.g., Bradley et al. 2008; Knudsen et al. 2017).

Considering the observed high- z quasars (QSOs) in the literature, in Bañados et al. (2019), for instance, the host galaxy of the QSO ULAS J1342 + 0928 at $z = 7.54$ showed a velocity gradient in which the northern part was blueshifted and the southern part was redshifted. In spite of this, the velocity dispersion did not resemble a coherent rotating structure. Hence, they interpreted the velocity dispersion structure as that of a merger. On the other hand, Shao et al. (2017) found that the velocity dispersion of a QSO at $z = 6.13$, with a best-fit inclination angle of 34° , has a coherent rotating structure that is consistent with the rotation of the galaxy. Similarly, Wang et al. (2013) observed six QSOs at $z \sim 6$ using ALMA and reported that their velocity gradients are consistent with rotating, gravitationally bound gas components.

For [C II] emitters, Smit et al. (2018) found rotating structures based on a simulation and their velocity fields in COS-3018555981 and COS-2987030247 at $z = 6.8$. Their results are consistent with rotationally supported galaxy disks, which were often found at $z \sim 2$. Likewise, Bakx et al. (2020) found a Lyman-break galaxy (LBG) (MACS0416-Y1) at $z \sim 8.3$ that shows a rotation-dominated disk given the observed velocity gradient. In addition, Hashimoto et al. (2019a) used ALMA and detected two clumps in B14-65666 at $z = 7.15$ with [O III] and [C II] emission lines. However, they thought that the galaxy is a starburst galaxy induced by a major merger because they did not see a smooth velocity field.

Given the complex velocity field of A1689-zD1 and the possibility that other dynamical interpretations would be equally valid as supported by the literature, further investigation is needed to make a conclusion. As mentioned in Section 3.3, A1689-zD1 may possibly be a merger with some northwestern ejected materials, or a merger with northwestern redshifted materials coming from a third, more highly obscured region of the galaxy.

5. Conclusions

Using the new ALMA Bands 6 and 8 data, we detect [C II] $158 \mu\text{m}$ and [O III] $88 \mu\text{m}$ emission lines for A1689-zD1. Our findings are summarized as follows.

1. We measure the redshift of A1689-zD1 as $z = 7.133 \pm 0.005$ based on [C II] and [O III] emission lines detected in Band 6 and Band 8 (natural and μv -tapered), respectively. The redshift is consistent with that adopted by Bakx et al. (2021).
2. Using the derived $L_{[\text{C II}]}$, we estimate a star formation rate of $\text{SFR}_{[\text{C II}], \text{Krou}} = 46.1 \pm 0.8 M_\odot \text{ yr}^{-1}$. Converting it from a Kroupa IMF into a Salpeter IMF, the value becomes $\text{SFR}_{[\text{C II}], \text{Sal}} = 68.8 \pm 1.2 M_\odot \text{ yr}^{-1}$, which is about a factor of 2 larger than the SED-fitting estimate $\text{SFR}_{\text{obs}, \text{Sal}} = 33 \pm 9 M_\odot \text{ yr}^{-1}$ in Bakx et al. (2021). However, the difference is still within a reasonable range according to Figure 4 of De Looze et al. (2011).
3. The [O III]/[C II] luminosity ratio of this galaxy is 2.09 ± 0.09 , which is similar to other high- z galaxies, but much higher than its local counterparts.
4. Despite a number of average $L_{[\text{O III}]} / L_{[\text{C II}]} \sim 2$, A1689-zD1 has an exceptionally high spatial ratio of $L_{[\text{O III}]} / L_{[\text{C II}]} \sim 7$ at the center of the galaxy. This is because [C II] emission is significantly spatially extended, while [O III] is compact at the center. Possible reasons of the compactness of [O III] include a central AGN, shock heating, and/or a starburst.
5. The moment-1 maps of the ALMA Bands 6 and 8 data (Figure 5) show complex velocity fields of A1689-zD1, with the northeastern part being blueshifted, the southwestern part being redshifted, and an additional northwestern part being comparatively more highly redshifted. It is therefore suggested that the galaxy may be a merger with the northwestern redshifted part being (1) some ejected material from the merger, or (2) some components coming from a third, more highly obscured region of the galaxy.












We are grateful to the anonymous referee for all the insightful comments. This paper makes use of the following ALMA data: ADS/JAO.ALMA#2015.1.01406.S and ADS/

JAO.ALMA#2017.1.00775.S. ALMA is a partnership of ESO (representing its member states), NSF (USA) and NINS (Japan), together with NRC (Canada), MOST and ASIAA (Taiwan), and KASI (Republic of Korea), in cooperation with the Republic of Chile. The Joint ALMA Observatory is operated by ESO, AUI/NRAO and NAOJ. Data analysis was in part carried out on the Multi-wavelength Data Analysis System operated by the Astronomy Data Center (ADC), National Astronomical Observatory of Japan. T.H. is supported by the Centre for Informatics and Computation in Astronomy (CICA) at National Tsing Hua University (NTHU) through a grant from the Ministry of Education of the Republic of China (Taiwan). T.G. and T.H. acknowledge the support by the Ministry of Science and Technology of Taiwan through grants 108-2628-M-007-004-MY3 and 110-2112-M-005-013-MY3, respectively. This research has made use of NASA's Astrophysics Data System.

Facilities: HST, ALMA.

Software: CASA (McMullin et al. 2007), astropy (Astropy Collaboration et al. 2013, 2018).

ORCID iDs

Yi Hang Valerie Wong  <https://orcid.org/0000-0001-6236-6882>
 Poya Wang  <https://orcid.org/0000-0003-2658-5871>
 Tetsuya Hashimoto  <https://orcid.org/0000-0001-7228-1428>
 Tomotsugu Goto  <https://orcid.org/0000-0002-6821-8669>
 Seong Jin Kim  <https://orcid.org/0000-0001-9970-8145>
 Alvina Y. L. On  <https://orcid.org/0000-0003-4479-4415>
 Daryl Joe D. Santos  <https://orcid.org/0000-0002-5687-0609>
 Ting-Yi Lu  <https://orcid.org/0000-0002-4965-6524>
 Ece Kilerci-Eser  <https://orcid.org/0000-0002-9119-2313>
 Simon C.-C. Ho  <https://orcid.org/0000-0002-8560-3497>
 Tiger Y.-Y. Hsiao  <https://orcid.org/0000-0003-4512-8705>

References

Astropy Collaboration, Price-Whelan, A. M., Sipőcz, B. M., et al. 2018, *AJ*, 156, 123
 Astropy Collaboration, Robitaille, T. P., Tollerud, E. J., et al. 2013, *A&A*, 558, A33

Bakx, T. J. L. C., Sommovigo, L., Carniani, S., et al. 2021, *MNRAS*, 508, L58
 Bakx, T. J. L. C., Tamura, Y., Hashimoto, T., et al. 2020, *MNRAS*, 493, 4294
 Bañados, E., Novak, M., Neeleman, M., et al. 2019, *ApJL*, 881, L23
 Bradley, L. D., Bouwens, R. J., Ford, H. C., et al. 2008, *ApJ*, 678, 647
 Carilli, C. L., & Walter, F. 2013, *ARA&A*, 51, 105
 Carniani, S., Ferrara, A., Maiolino, R., et al. 2020, *MNRAS*, 499, 5136
 Carniani, S., Maiolino, R., Pallottini, A., et al. 2017, *A&A*, 605, A42
 Cormier, D., Madden, S. C., Leboutteiller, V., et al. 2015, *A&A*, 578, A53
 De Looze, I., Baes, M., Bendo, G. J., Cortese, L., & Fritz, J. 2011, *MNRAS*, 416, 2712
 De Looze, I., Cormier, D., Leboutteiller, V., et al. 2014, *A&A*, 568, A62
 Díaz-Santos, T., Armus, L., Charmandaris, V., et al. 2017, *ApJ*, 846, 32
 Fujimoto, S., Ouchi, M., Ferrara, A., et al. 2019, *ApJ*, 887, 107
 Harikane, Y., Ouchi, M., Inoue, A. K., et al. 2020, *ApJ*, 896, 93
 Hashimoto, T., Inoue, A. K., Mawatari, K., et al. 2019a, *PASJ*, 71, 71
 Hashimoto, T., Inoue, A. K., Tamura, Y., et al. 2019b, *PASJ*, 71, 109
 Hopkins, P. F., Richards, G. T., & Hernquist, L. 2007, *ApJ*, 654, 731
 Howell, J. H., Armus, L., Mazzarella, J. M., et al. 2010, *ApJ*, 715, 572
 Inoue, A. K., Tamura, Y., Matsuo, H., et al. 2016, *Sci*, 352, 1559
 Jones, G. C., Carilli, C. L., Shao, Y., et al. 2017, *ApJ*, 850, 180
 Katz, H., Rosdahl, J., Kimm, T., et al. 2022, *MNRAS*, 510, 5603
 Knudsen, K. K., Watson, D., Frayer, D., et al. 2017, *MNRAS*, 466, 138
 Kroupa, P. 2001, *MNRAS*, 322, 231
 Laporte, N., Katz, H., Ellis, R. S., et al. 2019, *MNRAS*, 487, L81
 Madau, P., & Dickinson, M. 2014, *ARA&A*, 52, 415
 Madden, S. C., Rémy-Ruyer, A., Galametz, M., et al. 2013, *PASP*, 125, 600
 Malhotra, S., Helou, G., Stacey, G., et al. 1997, *ApJL*, 491, L27
 Matthee, J., Sobral, D., Boone, F., et al. 2017, *ApJ*, 851, 145
 McMullin, J. P., Waters, B., Schiebel, D., Young, W., & Golap, K. 2007, in ASP Conf. Ser. 376, *Astronomical Data Analysis Software and Systems XVI*, ed. R. A. Shaw, F. Hill, & D. J. Bell (San Francisco, CA: ASP), 127
 Minsley, R., Petric, A., Lambrides, E., et al. 2020, *ApJ*, 894, 157
 Novak, M., Bañados, E., Decarli, R., et al. 2019, *ApJ*, 881, 63
 Planck Collaboration, Ade, P. A. R., Aghanim, N., et al. 2016, *A&A*, 594, A13
 Shao, Y., Wang, R., Jones, G. C., et al. 2017, *ApJ*, 845, 138
 Silk, J. 1997, *ApJ*, 481, 703
 Smit, R., Bouwens, R. J., Carniani, S., et al. 2018, *Natur*, 553, 178
 Solomon, P. M., Downes, D., & Radford, S. J. E. 1992, *ApJL*, 398, L29
 Walter, F., Riechers, D., Novak, M., et al. 2018, *ApJL*, 869, L22
 Wang, R., Wagg, J., Carilli, C. L., et al. 2013, *ApJ*, 773, 44
 Watson, D., Christensen, L., Knudsen, K. K., et al. 2015, *Natur*, 519, 327
 Weibacher, P. M., Monreal-Ibero, A., Verhamme, A., et al. 2018, *A&A*, 611, A95
 Weinberg, S. 1972, *Gravitation and Cosmology: Principles and Applications of the General Theory of Relativity* (New York: Wiley)